JOURNAL OF Materials CHEMISTRY

Amorphous $FePO_4$ as 3 V cathode material for lithium secondary batteries

Young-Sik Hong,*[a] Kwang Sun Ryu,[a] Yong Joon Park,[a] Min Gyu Kim,[b] Jay Min Lee[b] and Soon Ho Chang[a]

[a]*Telecommunication Basic Research Lab., Electronics and Telecommunications Research Institute, 161 Gajeong-Dong, Daejeon 305-350, Korea. E-mail: youngsik@etri.re.kr; Fax: +82-42-860-6836; Tel: +82-42-860-5057*

[b]*Beamline Research Division, Pohang Accelerator Laboratory, Pohang University of Science and Technology, Pohang, 790-784, Korea*

Received 24th January 2002, Accepted 21st March 2002
First published as an Advance Article on the web 26th April 2002

The structural and electrochemical properties of amorphous $FePO_4 \cdot xH_2O$ (x = 2, 1, 0) and hexagonal $FePO_4$ powders have been investigated using differential thermal analysis–thermogravimetry (DTA–TGA), X-ray diffractometry (XRD), X-ray absorption spectroscopy (XAS), scanning electron microscopy (SEM), cyclic voltammetry (CV), and charge/discharge cycling. On heating, amorphous $FePO_4 \cdot 2H_2O$ was transformed into hexagonal $FePO_4$ at 380 °C, through amorphous $FePO_4 \cdot H_2O$ and $FePO_4$ phases. Reversible lithium insertion and extraction into and from the amorphous $FePO_4$ occurred at 2.8 and 3.2 V *vs.* Li/Li^+, respectively, which potentials are lower than those of the olivine-structured $LiFePO_4$. All samples show a large capacity loss at the 1st cycle, but their discharge capacities are gradually increased from 65 mA h g^{-1} (2nd cycle) to 75 mA h g^{-1} (15th cycle) at a current density of 17 mA g^{-1} and kept up to the 50th cycle. The discharge/charge dependence on the current densities (17, 34, and 85 mA g^{-1}) and operating temperatures (20, 50, and 80 °C) were also investigated for amorphous $FePO_4$. Fe K-edge X-ray absorption spectroscopy has been performed on amorphous Li_yFePO_4, to determine the changes in the local electronic and geometric structures during the discharge. For the Fe K-edge, the pre-edge and edge are shifted in accordance with the oxidation state of the Fe^{3+}/Fe^{2+} redox couple in Li_yFePO_4.

Introduction

Since the commercialization of the lithium ion battery by Sony Energetic, intensive efforts have been focused on the development of $LiNiO_2$, $Li(Ni,Co)O_2$, and $LiMn_2O_4$ as alternatives to the expensive and toxic cathode material $LiCoO_2$. Nevertheless, no practical transition metal oxides that satisfy the requirements of the lithium ion battery as well $LiCoO_2$ have yet been identified. In this regard, many investigators are searching for new cathode materials, such as fluorides, phosphates, sulfates, and inorganic–polymer composites, to substitute for lithium transition metal oxides. Of particular interest was an olivine-structured $LiFePO_4$ prepared by Padhi *et al.*[1] It was reported that olivine $LiFePO_4$ discharged at 3.4 V *vs.* Li/Li^+ and cycled well at ambient temperatures with a reversible capacity of 120 mA h g^{-1}. Subsequently, extensive work on such a phosphate material has been carried out by a number of groups.[2–11] Yamada *et al.* have recently reported that nearly full utilization of the theoretical capacity of $LiFePO_4$ at room temperature can be achieved by appropriate heat treatment.[3] This iron phosphate-based material is inexpensive, environmentally benign, and non-hygroscopic, compared to the lithium transition metal oxides.

One of the most important advantages of $LiFePO_4$ is that the energy state of the Fe^{3+}/Fe^{2+} redox couple is applicable to the lithium ion battery technology. The energy state of a redox couple depends on the electrostatic field of the active cations and the covalent contribution of the cation–anion bonding, resulting from the crystal structure and bonding character. From the viewpoint of the cell potential, the use of iron-based oxides as cathode material was ruled out, because the energy state of the Fe^{4+}/Fe^{3+} redox couple tends to lie far below the Fermi energy and that of the Fe^{3+}/Fe^{2+} is too close to it. In this respect, the substitution of oxygen by larger polyanions like $(XO_4)^{y-}$ (X = S, P, As, *etc.*) lowers the Fermi level of the Fe^{3+}/Fe^{2+} redox couple. It means that the strong X–O covalency in $(XO_4)^{y-}$ stabilizes the antibonding Fe^{3+}/Fe^{2+} state through an Fe–O–X inductive effect, leading to an increase in the cell potential.[1,2] Other phosphate–based materials such as $Li_2NaV_2(PO_4)_3$,[4] $Li(Fe_{1-x}Mn_x)PO_4$,[5] and $LiMPO_4$ (M = Co, Ni)[6,7] were also investigated. However, there are two main obstacles to improve electrochemical performance in these compounds: low diffusion rate and electronic conductivity. These problems are partly solved by preparing nanocrystalline powders with short diffusion distances and/or a composite material with a good electronic conductor.[8–13] For example, Nazar *et al.* reported that a $LiFePO_4$/C composite exhibited almost full capacity with good rate capability and excellent cyclability.[13]

In this paper, we report on the structural and electrochemical studies of the amorphous $FePO_4 \cdot xH_2O$ (x = 2, 1, 0; hereafter referred to as *a*-$FePO_4 \cdot xH_2O$) using TGA/DTA, XRD, XAS, SEM, CV, and charge/discharge cycling. The amorphous phase consists of nanocrystalline particles and shows significantly different structural and electrochemical behavior compared to the olivine-structured $LiFePO_4$.

Experimental

Sample preparation

The *a*-$FePO_4 \cdot xH_2O$ (x = 1, 0) and hexagonal $FePO_4$ powders were prepared by the heat treatment of commercially available $FePO_4 \cdot 2H_2O$ (Sigma-Aldrich) at various temperatures for 6 h in air.

 DOI: 10.1039/b200901c

Sample characterization

Differential thermal analysis (DTA) and thermogravimetric analysis (TGA) of $FePO_4{\cdot}2H_2O$ were performed using an SDT 2960 Simultaneous DTA–TGA (TA instruments) at the heating rate of 10 °C min^{-1} in air. To investigate the structure, the powders obtained were analyzed by X-ray diffraction (XRD) method using a MAC science MXP3A-HF diffractometer employing Cu Kα radiation. The scan data were collected in the 2θ range of 10–70°. The step size was 0.026° with a counting time of 3 s. Powder morphologies were obtained by field emission scanning electron microscopy (FE-SEM, Hitachi S-4300). The powders were coated with carbon by ion sputter (Hitachi E-1030). The accelerating voltage and emission current were 20 kV and 8000 nA, respectively.

Electrochemical characterization

Electrochemical experiments were performed in a Swagelock™ cell with lithium metal as the anode. The cathode pellet with 20% Super P carbon black and 5% PTFE was pressed and then dried at 120 °C for 2 h in a vacuum oven. The electrolyte used was 1 M $LiPF_6$ in 1 : 1 EC–DMC solution. All assemblage was carried out in an environmentally controlled dry room. Electrochemical properties were measured by a Biologic Mac Pile II charge/discharge cycler over the voltage range 4.3–2.0 V. The cyclic voltammetry was conducted at a scan rate of 30 $\mu V\ s^{-1}$. For an open-circuit voltage measurement, the cell was discharged to 2.0 V at the current density of 3 mA g^{-1} and the current was intermittently switched off at 0.1 V intervals during the discharge. The standing time for equilibration was 6 h. The cell was also cycled in a thermostatically controlled environmental chamber (Vötsch VC7018) maintained at either 50 or 80 °C.

X-Ray absorption measurement

To analyze the changes of electronic and geometric structures of Fe^{3+}/Fe^{2+} in the a-Li_yFePO_4, the cathode pellets were recovered after discharging the cells to specified voltages. Fe K-edge X-ray absorption spectra were recorded on the BL3C1 beam line of a Pohang Light Source (PLS) with a ring current of 120–170 mA at 2.5 GeV. A Si(111) monochromator crystal was used with detuning to 85% in intensity to eliminate the high-order harmonics. The data were collected with nitrogen gas-filled ionization chambers in transmission mode. Energy calibration was carried out with Fe metal foil, where the first inflection point was assigned to 7112 eV. In order to remove an energy shift problem, the X-ray absorption spectrum of Fe metal foil was measured simultaneously.

The EXAFS data analysis was carried out by the standard procedure reported elsewhere.[14] The measured absorption spectra below the pre-edge region were fitted to a straight line, and then the background contribution above the post-edge region, $\mu_o(E)$, was fitted to the 4th order polynomial (cubic spline) and extrapolated throughout the whole energy region. The fitted polynomial was subtracted from the absorption spectra. The background-subtracted absorption spectra were normalized according to the equation, $\chi(E) = \{\mu(E)\mu_o - (E)\}/\mu_o(E)$. The normalized k^3-weighted EXAFS spectra, $k^3\chi(k)$, were Fourier transformed in the k range from 2.8 to 14.0 $Å^{-1}$. The experimental Fourier-filtered $k^3\chi(k)$ spectra were obtained from the inverse Fourier transformation with the Hanning window function in the r space range between 1.0 and 6.0 Å. In order to determine the structural parameters for each bond pair, the curve fitting process was carried out by using the EXAFS formula, which can be expressed as follows: $\chi(k) = \Sigma N_j S_i^2(k) F_j(k) \exp(-2\sigma_j^2 k^2) \exp(-2r_j/\lambda_j(k)) [\sin(2kr_j + \Phi_{ij}(k))/kr_j^2]$, where the photoelectron wave vector, $k = [8\pi^2 m(E - E_o)/h^2]^{1/2}$, the coordination number is N_j, the atom loss factor, S_i^2, the effective curved wave backscattering amplitude, $F_j(k)$, the Debye–Waller factor, σ_j^2, the mean free path of the photoelectron, λ, the interatomic distance, r_j, and total phase shift, Φ_{ij}, respectively.

Theoretical scattering paths are obtained from the crystallographic description of the known structural model. The theoretical EXAFS parameters, such as phase shift, backscattering amplitude, and atom loss factor, have been calculated for all possible scattering paths by FEFF6.01 code. The coordination number (N) was also fixed to the crystallographic data of polycrystalline $LiFePO_4$[7] since the N value is highly correlated with the Debye–Waller factor in the amplitude of EXAFS spectra. The experimental $k^3\chi(k)$ spectra were fitted with possible scattering paths showing the substantial amplitude for the corresponding FT peak.

Results and discussion

Thermal behavior of pristine a-$FePO_4{\cdot}2H_2O$

The DTA–TGA curves of pristine a-$FePO_4{\cdot}2H_2O$ are given in Fig. 1. The two large endothermic peaks around 115 and 142 °C with the weight loss of 18% correspond to the elimination of two water molecules. It is noteworthy that the weight losses in each step approximately correspond to one water molecule as shown in the deconvolution curves, which are carried out by a multiple Gaussian function in the Origin 6.0 (Microcal Software Inc.) Professional Program. This indicates that the water molecules in a-$FePO_4{\cdot}2H_2O$ are dehydrated by two successive steps as follows:

$$FePO_4{\cdot}2H_2O \xrightarrow{-H_2O} FePO_4{\cdot}H_2O \xrightarrow{-H_2O} FePO_4$$

As the calcination temperature was raised to around 380 °C, a broad endothermic peak appeared, which may be from the structural transformation from a-$FePO_4$ into hexagonal $FePO_4$, as confirmed by XRD analysis (Fig. 2). At the temperature range 540–630 °C, a couple of peaks due to the decomposition were observed.

Structural analysis

The XRD patterns of the samples prepared at different temperatures are shown in Fig. 2. The pristine a-$FePO_4{\cdot}2H_2O$ shows completely amorphous character, which it keeps up to 350 °C, irrespective of water content. The amorphous phases are completely different from the crystalline $FePO_4{\cdot}2H_2O$ (JCPDS No. 33-0666) or olivine $FePO_4$ (a = 5.792, b = 9.821, and c = 4.788 Å).[1] Close inspection of the XRD patterns shows that the broad diffraction peak of a-$FePO_4$ was shifted to a lower angle (~2 deg) than those of a-$FePO_4{\cdot}2H_2O$ and a-$FePO_4{\cdot}H_2O$. One can assume that the pristine a-$FePO_4{\cdot}2H_2O$ has two different sites for water molecules, as shown by the two

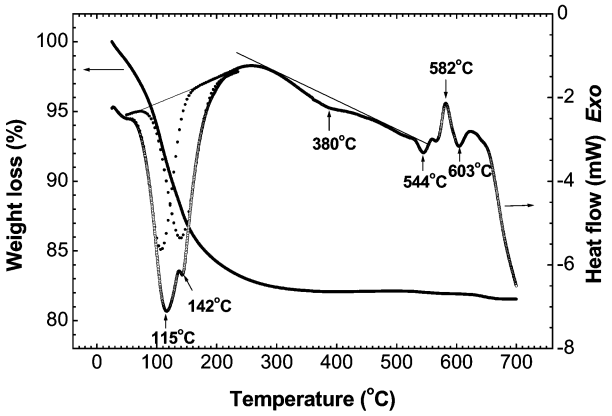

Fig. 1 DTA–TGA curves for the amorphous $FePO_4{\cdot}2H_2O$ in air.

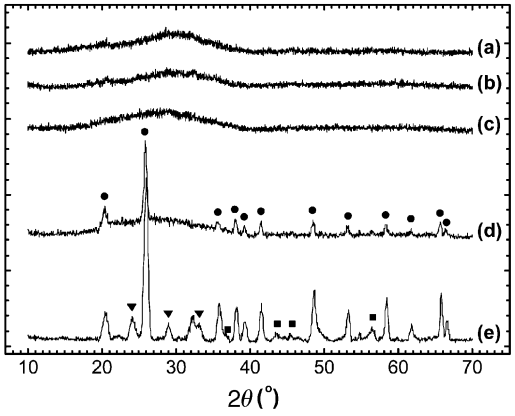

Fig. 2 X-Ray diffraction patterns of (a) pristine $FePO_4 \cdot 2H_2O$ and the samples prepared at different temperatures of (b) 120 °C, (c) 350 °C, (d) 500 °C, and (e) 600 °C. (●: hexagonal $FePO_4$, ■: Fe_3PO_7, ▼: $Fe_4(P_4O_{12})_3$).

DTA peaks. The XRD patterns of the sample prepared at 500 °C show the diffraction peaks of hexagonal $FePO_4$ to be well developed on top of the broad hump, indicating the transformation from *a*-$FePO_4$ to hexagonal $FePO_4$ (JCPDS No. 31-0647). At 600 °C, the hexagonal $FePO_4$ had begun to decompose to $Fe_4(P_4O_{12})_3$ (JCPDS No. 38-0052) and Fe_3PO_7 (JCPDS No. 37-0061).

Discharge/charge cycles of *a*-$FePO_4 \cdot xH_2O$ ($x = 2, 0$) and hexagonal $FePO_4$

Investigations of the lithium insertion behavior were electrochemically carried out on the *a*-$FePO_4 \cdot xH_2O$ ($x = 2, 0$) and hexagonal $FePO_4$ phases. The initial five discharge/charge cycles at the current density of 17 mA g^{-1} and voltage limits of 4.3–2.0 V are shown in Fig. 3. Note that the capacities of *a*-$FePO_4 \cdot xH_2O$ begin to slightly increase from the 2nd discharge cycle even though they are small. The reason for such a result is not clear; it could come from the electrochemical grinding effect of the cathode particles as observed in Li_xMVO_4 (M = Zn, Ni, Cd)[15] and/or the gradual contribution of lithium ions trapped in the 1st discharge step. Among the three samples, the discharge capacities of pristine *a*-$FePO_4 \cdot 2H_2O$ showed the highest value of around 76 mA h g^{-1} at the 2nd cycle (Fig. 3, inset), but most of the cells fabricated with *a*-$FePO_4 \cdot 2H_2O$ failed within twenty cycles. Meanwhile, the

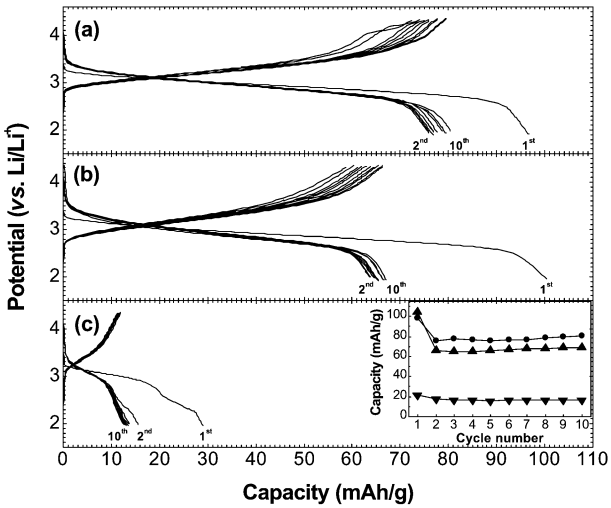

Fig. 3 Discharge/charge curves for (a) pristine $FePO_4 \cdot 2H_2O$ (●) and the samples prepared at (b) 350 °C (▲) and (c) 500 °C (▼). Inset shows the plot of discharge capacities *versus* cycle number.

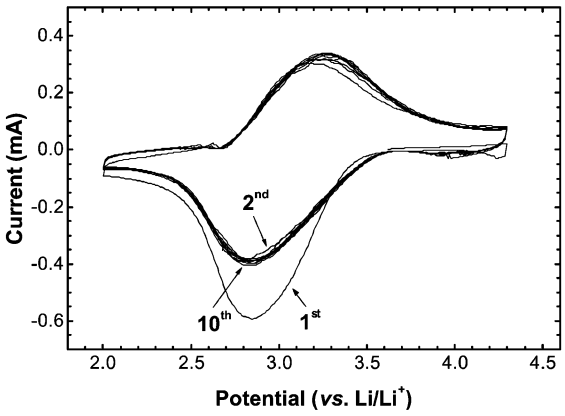

Fig. 4 Cyclic voltammograms for amorphous $FePO_4$ at a scan rate of 30 μV s^{-1}.

sample prepared at 500 °C exhibits only 13% electrochemical activity of theoretical capacity, resulting from the unconverted *a*-$FePO_4$, as shown in the XRD profile. This means that the hexagonal $FePO_4$ is electrochemically inactive. Therefore, we will concentrate on the change of the electrochemical properties and electronic states of *a*-$FePO_4$ prepared at 350 °C since it shows the best electrochemical performances from the viewpoints of capacity and cyclability.

Electrochemical properties of *a*-$FePO_4$

The cyclic voltammogram of *a*-$FePO_4$ at a scan rate of 30 μV s^{-1} is presented in Fig. 4. It exhibits one reduction peak spreading from 2.7 to 3.8 V and one oxidation peak from 2.5 to 3.6 V, where average voltage between reduction and oxidation is almost 3.0 V. This indicates that the electrochemical insertion/extraction of lithium ions proceeds through a large number of successive *a*-Li_yFePO_4 phases without any formation of crystalline phases. In fact, the XRD patterns of the discharged cathode pellets *a*-Li_yFePO_4 ($0 \leqslant y \leqslant 0.72$) showed only broad amorphous peaks (not shown here). The open-circuit voltage (OCV) and closed-circuit voltage (CCV) curves of *a*-$FePO_4$ are shown in Fig. 5. Under equilibrium conditions, 0.90 lithium ions per formula unit can be inserted into the cathode material while 0.68 lithium ions are inserted in CCV mode. This observation indicates that the insertion of lithium ions in the *a*-$FePO_4$ is kinetically limited.

The cycling tests were performed on different current densities and operating temperatures. The discharge capacities are shown in Fig. 6. For all samples, the difference between the 1st and 2nd discharge capacities is very detrimental to the subsequent cycles. Normally, it has been reported that the discharge capacity of the $LiFePO_4$ electrode is limited by the diffusion rate of the lithium ions in the $LiFePO_4$ particles.[9]

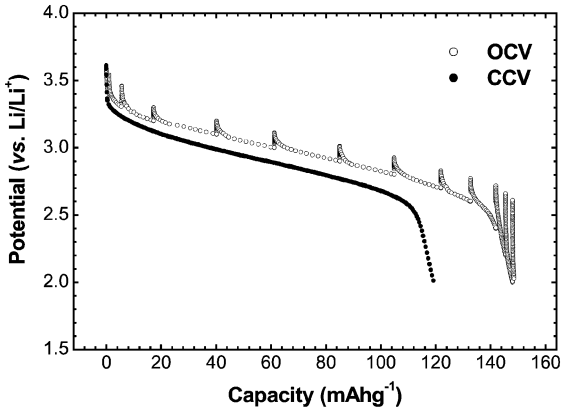

Fig. 5 Open-circuit voltage measured for amorphous $FePO_4$.

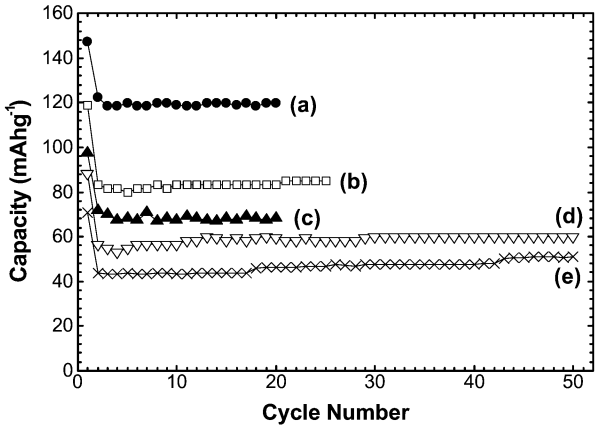

Fig. 6 Discharge capacity *vs.* current density as a function of current densities and operating temperatures. (a) 85 mA g^{-1} at 80 °C, (b) 85 mA g^{-1} at 50 °C, (c) 170 mA g^{-1} at 50 °C, (d) 34 mA g^{-1} at 20 °C, and (e) 85 mA g^{-1} at 20 °C.

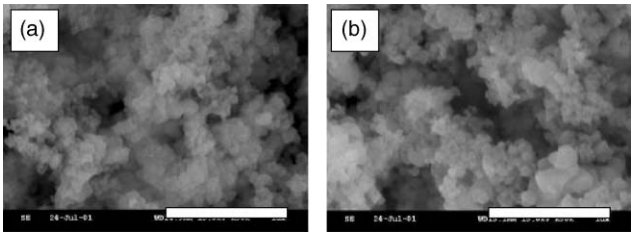

Fig. 7 Scanning electron micrograph of (a) pristine $FePO_4 \cdot 2H_2O$ and (b) amorphous $FePO_4$ (bar = 1 μm).

In this respect, it is a bit strange that the discharge capacity is not greatly improved even though the *a*-$FePO_4$ powders consist of nanocrystals between 50 and 200 nm (Fig. 7). It indicates that the most important factor in increasing the capacity of the *a*-$FePO_4$ is not the diffusion behavior but the electronic conductivity. We examined the effect of the operating temperature since the high-temperature behavior of a battery is also an important factor. The discharge capacity of the cell was increased as the operating temperature was raised. At 80 °C, the initial discharge capacity reached 147 mA h g^{-1} at a current density of 85 mA g^{-1}. Although a large capacity loss of ~30 mA h g^{-1} occurs in the 2nd cycle, the remaining capacity is maintained up to the 20th cycle. Compared to Li_yFeVO_4,[16] where the lithiation into $FeVO_4$ irreversibly occurs through a single phase at $0 < y < 0.3$, *a*-$FePO_4$ shows a much better electrochemical performance. The excellent cyclic performance may be related to the amorphous character of *a*-$FePO_4$, which mitigates the structural change that gives rise to contact loss and capacity fade.

Fe K-edge X-ray absorption near edge structure (XANES) analysis

Fig. 8 shows the Fe K-edge XANES spectra for the *a*-Li_yFePO_4 (y = 0, 0.15, 0.33, 0.52, 0.66, and 0.72), where y values are calculated from the electric charges. The Fe K-edge XANES spectra for the *a*-Li_yFePO_4 effectively change with the lithium ion content. The position and shape of the edge and pre-edge peaks are closely related to the oxidation state of the absorbing ion and the local arrangement of backscattering ions. Compared to Fe_2O_3 and FeO, the edge shift of *a*-Li_yFePO_4 clearly shows the changes of oxidation state of Fe^{3+}/Fe^{2+} with the lithium ion insertion. In the pre-edge region, as the lithium ion inserts, the intensity of peak A decreases gradually while an additional peak B develops in the region of ~2 eV lower energy than peak A. The pre-edge peak A at ~7114 eV represents the transition of a core 1s electron to an unoccupied 3d orbital of

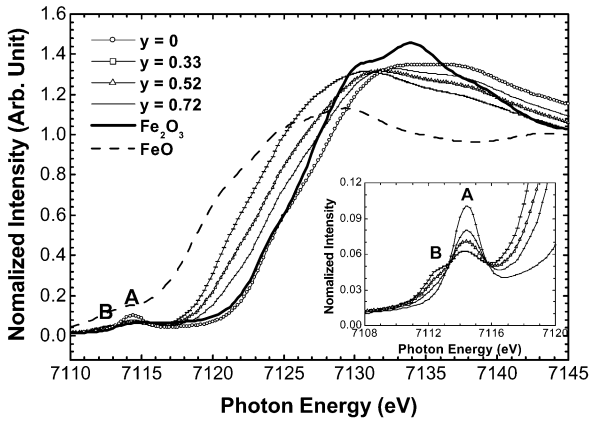

Fig. 8 Fe K-edge XANES spectra for amorphous Li_yFePO_4.

Table 1 Peak position, width, and area for Fe K-edge XANES spectra of *a*-Li_yFePO_4[a]

	A peak		B peak	
Compound	Width	Area	Width	Area
$FePO_4$	1.03	0.15	—	—
$Li_{0.15}FePO_4$	1.09	0.10	1.09	0.010
$Li_{0.33}FePO_4$	1.07	0.09	1.07	0.013
$Li_{0.52}FePO_4$	1.08	0.06	1.08	0.018
$Li_{0.66}FePO_4$	1.04	0.04	1.04	0.024
$Li_{0.72}FePO_4$	1.05	0.04	1.05	0.025

[a]Each peak was fitted with the Lorentzian function, $f(E) = 2A\Gamma/\pi\{\Gamma^2+4(E - E_c)^2\}$, where E, A, and Γ represent peak position, peak area, and full width at half maximum (FWHM) of the peak, respectively.

the Fe^{3+} ion. Although the 1s → 3d transition is an electric dipole-forbidden transition in an ideal octahedral symmetry, the absorption peak appears due to pure electric quadrupole coupling and the noncentrosymmetric environment of the slightly distorted Fe octahedral site. Peak B is assigned to the transition to an unoccupied 3d orbital of the Fe^{2+} ion since the lower absorption energy is necessary for the more reduced Fe ion because of the deshielding effect for the 1s core electron. Then, this fact directly shows that the Fe^{3+} state decreases and in turn the Fe^{2+} state increases as the lithium ion is inserted into the *a*-$FePO_4$. The peak widths and areas for the Fe K-edge XANES spectra of *a*-Li_yFePO_4 are listed in Table 1, in order to present the relationship between the A : B peak intensity ratio and the lithium ion content. The linear relationship shows that the peak intensity is proportional to the lithium ion content within the *a*-Li_yFePO_4.

Fe K-edge extended X-ray fine structure spectroscopy (EXAFS) analysis

Since the EXAFS spectral change is indicative of the local structural variation around Fe atom, it is of interest to quantitatively determine the changes in local structure using Fe K-edge EXAFS. The Fourier transforms (FTs) obtained from the experimental k^3-weighted Fe K-edge EXAFS spectra are represented in Fig. 9. For the *a*-$FePO_4$, the first FT maximum at ~1.5 Å corresponds to the nearest neighboring oxygens around the Fe, while the other FT maxima above 2.1 Å are considered as the contributions by more highly coordinated atoms such as P and Fe. No FT peak was observed around 3.5 Å. This means that the local structure around the Fe atom in *a*-$FePO_4$ is clearly different from that in olivine $LiFePO_4$, since olivine $LiFePO_4$ has an Fe–Fe interatomic distance of ~3.5 Å.[6] Meanwhile, the local structure of *a*-$FePO_4$ is more close to that of *a*-$Fe_3(P_2O_7)_2$ with pyrophosphate groups since

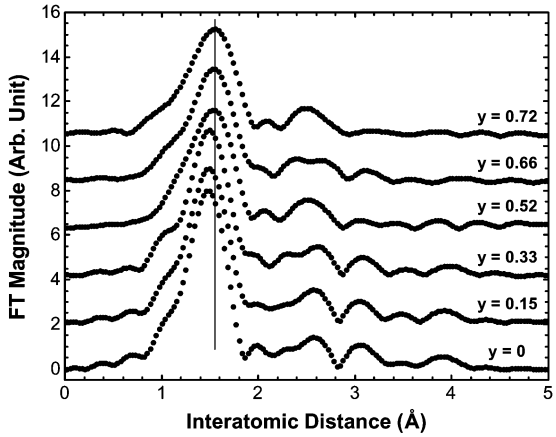

Fig. 9 Fourier-transformed Fe K-edge EXAFS spectra for the amorphous Li_yFePO_4.

Table 2 Fe K-edge EXAFS parameters for electrochemically lithium inserted *a*-Li_yFePO_4[a]

Compound	Shell	N	ΔE/eV	R/Å	$\sigma^2 \times 10^{-3}$/Å^2
$FePO_4$	Fe–O	6	3.4	1.92	4.8
$Li_{0.15}FePO_4$	Fe–O	6	3.3	1.94	6.4
$Li_{0.33}FePO_4$	Fe–O	6	3.1	1.95	6.5
$Li_{0.52}FePO_4$	Fe–O	6	2.8	1.98	7.2
$Li_{0.66}FePO_4$	Fe–O	6	2.7	2.00	7.7
$Li_{0.72}FePO_4$	Fe–O	6	2.7	2.02	7.9

[a]In all curve fitting process, the goodness of fit by $\{\Sigma(k^3\chi_{data} - k^3\chi_{model})^2\}/\Sigma(k^3\chi_{data})^2$ has been estimated within the allowed error range. The estimated errors are within ± 0.02 Å for the interatomic distance and 15% for the Debye–Waller factor.

the significant FT peak of ~2.0 Å abruptly decreases in *a*-$Fe_3(P_2O_7)_2$ as well as *a*-$FePO_4$.[17] Relating to the electrochemistry, it can be supported by the fact that the energy states of the Fe^{3+}/Fe^{2+} redox couple in $LiFeP_2O_7$ (2.9 V) and $Fe_4(P_2O_7)_3$ (3.1 V) with pyrophosphate groups are closer to the *a*-$FePO_4$ than the olivine $LiFePO_4$.

The Fe K-edge EXAFS spectra have also changed considerably with respect to the lithium ion insertion. The FT peak for the 1st scattering pair of Fe–O shifts to the higher distance region and the peak intensity decreases systematically with the y value. Although the 1st FT peak of the Li_yFePO_4 includes three kinds of Fe–O bond pairs, the structural refinement has been carried out with one shell model for clarity. The Fe K-edge EXAFS parameters for Li_yFePO_4 are listed in Table 2. The average interatomic distance of the Fe–O bond increases linearly with lithium ion insertion from 1.92 to 2.02 Å. It is reasonable because lithium ion insertion leads to the reduction of Fe^{3+} to Fe^{2+}, as shown in the XANES features. Now we can correlate the Fe^{3+}/Fe^{2+} redox potential and the bond distance of Fe–O in the *a*-$FePO_4$ and olivine $LiFePO_4$. That is, the redox potential of *a*-$FePO_4$ may be lower than that of olivine $LiFePO_4$, since the bond distance (1.92 Å) of Fe–O in the *a*-$FePO_4$ is shorter than that (2.03 Å) of olivine $FePO_4$.[11]

As the lithium ions are inserted, the coordination number of the Fe atoms is decreased and the Debye–Waller factor is increased systematically. The magnitude of the FT peak is inversely related to the Debye–Waller factor that corresponds to the mean square relative displacement (MSRD) of interatomic distance for each Fe–O bond pair due to static disorder and thermal vibrational disorder. In Li_yFePO_4, the systematic decrease of FT magnitudes results from the major contribution of static disorder, mainly associated with the two different oxidation state Fe^{2+} and Fe^{3+} ions.

Conclusion

The present work describes the structural and electrochemical properties of *a*-$FePO_4 \cdot xH_2O$ obtained from the heat treatment of pristine *a*-$FePO_4 \cdot 2H_2O$. According to the Fe K-edge XAS results, it can be concluded that the electrochemical insertion of lithium ions is related to the redox reaction of Fe^{3+}/Fe^{2+} and the cell potential is dependent on the Fe–O bond distance. Although the capacity and cell potential are unfortunately inferior to those of $LiFePO_4$, it can be included as a new 3 V cathode material in lithium ion rechargeable batteries. Very recently, Croce *et al.* suggested that the cell composed of a lithium metal anode, a PEO-based polymer electrolyte, and a phospho-olivine cathode could be utilized for electric vehicle operation.[18] In line with this, the *a*-$FePO_4$ can be considered as an alternative to lithium transition metal oxides for a special purpose because of its good cyclic performance at higher operating temperatures. One of the most encouraging advantages is that the *a*-$FePO_4$ is to easy prepare while the undesirable particle growth and the presence of residual Fe^{3+} phase happen in the olivine $LiFePO_4$.

Acknowledgement

This work was supported by the Ministry of Information and Communication in Korea.

References

1 A. K. Padhi, K. S. Nanjundaswamy and J. B. Goodenough, *J. Electrochem. Soc.*, 1997, **144**(4), 1188.
2 J. B. Goodenough, A. K. Padhi, K. S. Nanjundaswamy and C. Masquelier, *US Pat.*, 5910382, 1999.
3 A. Yamada, S. C. Chung and K. Hinokuma, *J. Electrochem. Soc.*, 2001, **148**(3), A224.
4 B. L. Cashing and J. B. Goodenough, *J. Solid State Chem.*, 2001, **162**, 162.
5 A. Yamada, Y. Kudo and K.-Y. Liu, *J. Electrochem. Soc.*, 2001, **148**(7), A747.
6 S. Okada, S. Sawa, M. Egashira, J. Yamaki, M. Tabuchi, H. Kageyama, T. Konishi and A. Yoshino, *J. Power Sources*, 2001, **97–98**, 430.
7 O. García-Moreno, M. Alvarez-Vega, F. García-Alvarado, J. García-Jaca, J. M. Gallardo-Amores, M. L. Sanjuán and U. Amador, *Chem. Mater.*, 2001, **13**, 1570.
8 K. Amine, H. Yasuda and M. Yamachi, *Electrochem. Solid-State Lett.*, 2000, **3**(4), 178.
9 A. S. Andersson, B. Kalska, L. Häggström and J. O. Thomas, *Solid State Ionics*, 2000, **130**, 41.
10 A. S. Andersson, J. O. Thomas, B. Kalska and L. Häggström, *Electrochem. Solid-State Lett.*, 2000, **3**(2), 66.
11 A. S. Andersson and J. O. Thomas, *J. Power Sources*, 2001, **97–98**, 498.
12 R. Nathalie, B. Simon, S. Martin, V. Alain, A. Michel and M. Jean-François, EP 1049182A2, 2000.
13 L. F. Nazar, G. Goward, F. Leroux, M. Duncan, H. Huang, T. Kerr and J. Gaubicher, *Int. J. Inorg. Mater.*, 2001, **3**, 191.
14 N. Treuil, C. Labrugere, M. Menetrier, J. Portier, G. Campet, A. Deshayes, J. C. Frison, S. J. Hwang, S. W. Song and J. H. Choy, *J. Phys. Chem. B*, 1999, **103**, 2100.
15 D. Guyomard, C. Sigala, A. Le Gal La Salle and Y. J. Piffard, *J. Power Sources*, 1997, **68**, 692.
16 M. Hayashibara, M. Eguchi, T. Miura and T. Kishi, *Solid State Ionics*, 1997, **98**, 119.
17 G. K. Marasinghe, M. Karabulut, C. S. Ray, D. E. Day, M. G. Shumsky, W. B. Yelon, C. H. Booth, P. G. Allen and D. K. Shuh, *J. Non-Cryst. Solids*, 1997, **222**, 144.
18 F. Croce, F. Serraino Fiory, L. Persi and B. Scrosati, *Electrochem. Solid-State Lett.*, 2001, **4**(8), A121.